ELSEVIER

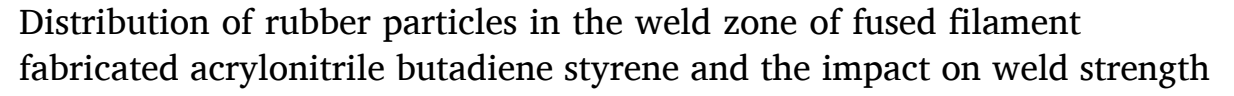
Contents lists available at ScienceDirect

Additive Manufacturing

journal homepage: www.elsevier.com/locate/addma



Research Paper



David W. Collinson ^{a,1}, Pavan V. Kolluru ^b, Natalia Von Windheim ^c, L. Catherine Brinson ^{c,*}

- ^a Department of Mechanical Engineering, Northwestern University, Evanston, IL 60208, USA
- ^b Materials Science and Engineering Department, Texas A&M University, College Station, TX 77843, USA
- ^c Department of Mechanical Engineering and Materials Science, Duke University, Durham, NC 27708, USA

ARTICLE INFO

Keywords:

Atomic force microscopy Additive manufacturing Acrylonitrile butadiene styrene Fused Filament Fabrication Weld strength

ABSTRACT

Fused filament fabrication (FFF) is a common additive manufacturing method for polymers that has been widely adopted due to its low cost and ease of use. However, FFF remains limited in high performance applications due to the weak mechanical properties of the welds between printed fibers, including for parts manufactured from acrylonitrile butadiene styrene (ABS). This study uses atomic force microscopy (AFM) to obtain high resolution nanomechanical maps of the distribution of butadiene particles around weld interfaces in FFF-ABS specimens. From quantitative image analysis, a decrease in the average size and density of the polybutadiene particles is observed within a 5–10 µm region across multiple welds. We find that the lack of craze-inducing polybutadiene particles within the weld zone promotes brittle fracture between printed fibers and results in a reduced weld strength as measured by trouser tear experiments. To improve the fracture toughness of FFF-ABS, methods to promote particle migration into the weld region during or after printing could be considered.

1. Introduction

Additive manufacturing has emerged as a new paradigm in the rapid development and manufacture of engineering components [1]. Compared to conventional methods, additive manufacturing is attractive due to its ability to manufacture complex geometries, with reduced design-to-fabrication times and material wastage [1,2]. Specifically, in fused filament fabrication (FFF), a molten polymer filament is extruded through a heated nozzle and deposited onto the substrate, to create a layer of the polymer (Fig. 1(a)). Upon deposition, the molten filaments relax and weld with their neighbors within the layer as well as with filaments in the preceding layer, thus leading to the formation of single cohesive part as shown in the inset of Fig. 1(a). The nature of the filament deposition in FFF leads to significant porosity or air gaps between deposited filaments as can be observed in Fig. 1(b). Application of functional FFF components remains limited as the mechanical performance of polymer components made via FFF often cannot compete with similar components manufactured through conventional means such as injection molding [3].

The local contact regions between filaments, also known as the neck/

weld regions (Fig. 1(c)), are responsible for stress transfer across filaments and critical to the strength of an FFF part [4,5]. Manufacturing parameters, such as thermal history and material parameters of the feedstock, affect the overall strength of a part, particularly through their impact on the filament-filament bonding strength in the weld regions [3, 4,6-8]. Bond development between neighboring filaments is typically described as a diffusion controlled process that involves heating of the part above the polymers glass transition temperature to allow translation of polymer chains and growth of the contact region between two filaments across the interface before cooling the polymer [5,9]. However, some other recent work has suggested that the mechanical strength of the weld is a product of weld geometry [10] and changes in polymer structure near the weld [11]. During FFF, a weld region undergoes repeated heating-cooling cycles as the filament is laid down by the printer, followed by neighboring filaments in the same layer, and then eventually another series of heating-cooling cycles as the next layer of material is placed on top [5,9,12]. Finally, another heating cycle may occur if a post printing annealing step is included. Additionally, the location of the filament in the printed part, location in the printing chamber, whether a heated bed or chamber is used, can all affect the

E-mail addresses: davidcollinson2020@u.northwestern.edu (D.W. Collinson), pavan.kolluru@tamu.edu (P.V. Kolluru), natalia.von.windheim@duke.edu (N. Von Windheim), cate.brinson@duke.edu (L.C. Brinson).

^{*} Corresponding author.

¹ Current address: Department of Materials Science, Stanford University, Stanford, CA 94305, USA.

thermal history of the part.

Acrylonitrile butadiene styrene (ABS) is an amorphous, ternary polymer commonly used for FFF that is comprised of a poly(styrene-coacrylonitrile) (SAN) matrix with nitrile-butadiene rubber particles that range between 50 nm and 1.5 µm in diameter (D) dispersed throughout [13]. The size of the rubber domains/particles used to toughen SAN and other glassy polymers has been shown to significantly impact the fracture toughness and mechanical properties of ABS and other rubber-modified polymers [14]. Effective toughening of glassy polymers with compliant particles generally requires that the particle diameter exceeds a critical diameter to effectively induce craze formation at stresses lower than the brittle fracture stiffness of the matrix [15,16]. For ABS, a bimodal distribution of polybutadiene particles has been demonstrated to produce the most effective toughening [17-20]. The larger butadiene particles toughen the stiff and brittle SAN matrix by serving as initiation sites for craze formation under a flow stress that allows for significant plastic deformation before failure of the SAN matrix [15]. Meanwhile, the inclusion of smaller polybutadiene particles in addition to the craze-inducing large particles has been suggested to improve the fracture toughness of ABS further by stabilizing the craze growth induced by large particles through particle cavitation and initiation of shear yielding in the SAN matrix [19,20]. If either of the large or small butadiene particles are not present, the fracture toughness of ABS suffers as a result.

The overall strength, stiffness and failure mechanisms of FFF-ABS printed parts is dependent on a wide range of factors such as layer thickness, feed rates, printing location, raster speed, printing temperature, cooling rates, part infill, raster pattern and orientation, and air gap size [21]. Recent work by Hart et al. [22,23], on the fracture behavior with FFF-printed ABS parts have demonstrated that a weak inter-laminar region is the primary cause for the poor critical fracture energy release rate of $G_{\rm Ic}=260~{\rm J/m^2}$. In comparison, injection-molded ABS has been measured to have $G_{\rm Ic}=4000~{\rm J/m^2}$. For the FFF specimens, crack growth was shown preferentially grow along the interfaces and cause a part to fail prematurely in a brittle manner. Cole et al. [24]. determined by nano-indentation that the interfacial 'neck' region was stiffer than the bulk of the fiber in FFF-ABS. The increase in stiffness was associated with a decrease in the butadiene/styrene ratio in the interfacial region as measured by Raman spectroscopy suggesting that the

increase in local stiffness was the result of low polybutadiene concentration within the weld region. A localized decrease in polybutadiene particle concentration within the weld region may explain the poor interlaminar fracture toughness as the polybutadiene particles essential for improving fracture toughness of an otherwise brittle SAN matrix are absent.

While previous studies have identified that the weld region in FFF printed parts is significantly weaker than expected from bulk properties, little work has been done to directly connect the change in fracture toughness to the underlying microstructure and distribution of the polybutadiene particles. This study seeks to improve our understanding of the ABS microstructure in the weld region of FFF parts and how it may influence the fracture toughness of the part. Atomic force microscopy (AFM) is used in this study to provide high-resolution, nanoscale mechanical property maps of the ABS microstructure and mechanical properties near the weld zone between printed filaments. From the acquired images, quantitative analysis of the butadiene distribution is used to determine whether the particle density is altered within the weld zone and establish whether the changes can be connected to trouser tear tests of the weld strength.

2. Materials and methods

2.1. Materials

All specimens were printed using ABS m30i (Stratasys, USA) on a Fortus 250mc (Stratasys, USA) with a nozzle temperature of 255 $^{\circ}$ C, the chamber heated to 70 $^{\circ}$ C and a layer thickness of 330 μ m. A thin-walled cylindrical specimen was used for tear testing and high-resolution AFM analysis to simplify thermal history and allow for the isolation of single welds. All tear testing samples were taken from a single printed cylinder that was also used to prepare samples for AFM to ensure that the tearing data reflected the thermal history of the welds imaged with AFM as closely as possible. In addition, all tear testing and AFM samples were extracted from the cylinder while avoiding the bottom 15 mm that could have a thermal history modified due to proximity to the heated print bed. The printed cylinder was 50 mm in diameter and 200 mm tall with the central axis of the cylinder perpendicular to the build plate. After printing, the cylinder walls were measured to be approximately 700 μ m

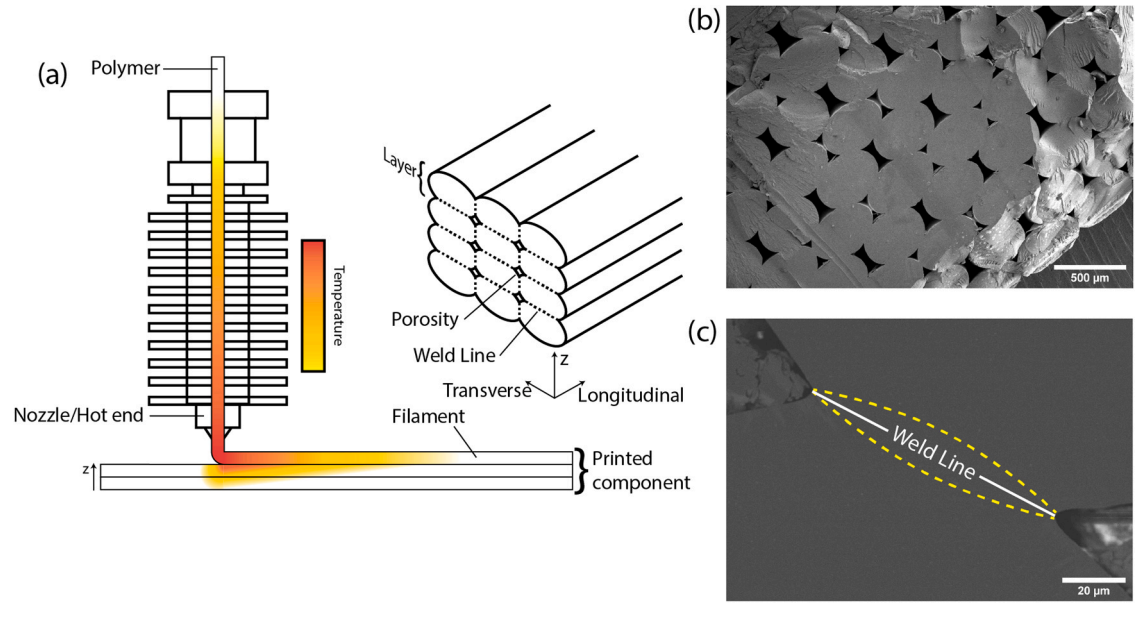


Fig. 1. (a) Schematic of fused filament fabrication and the resulting structure of the printed component. (b) Scanning electron microscopy (SEM) image of the cross section in a FFF-ABS specimen. (c) SEM image of the neck region between two printed fibers. The weld line is defined as the shortest distance between the air gaps on either side of the printed fibers.

thick and each layer consisted of two filaments lying side-by-side. For a representative bulk sample, a dog bone specimen was printed to dimensions conforming to ASTM D638-03 (Type I) lying flat on the build plate [25]. The specimen was printed with 100% infill and the fiber direction parallel to the long axis of the dog bone.

To prepare the cylindrical sample for AFM, sections were cut from the printed cylindrical samples using a diamond saw and then a surface for AFM analysis that included the weld interfaces between three fibers was sectioned at $-120~^\circ\text{C}$ with a UC7 Ultramicrotome (Leica, Germany) to produce a smooth surface and preserve the butadiene particle structure, with an $R_a=1.7~\text{nm}$ as measured by AFM on the SAN matrix. Prior to cryotoming, cyanoacrylate glue was used to fill the air gaps between fibers to allow for scanning across the inter-fiber porosity without the AFM tip disengaging from the surface.

The bulk sample was prepared by first freeze fracturing the printed dog bone to expose the internal fibers. The internal cross section was then polished and gently ion milled using an EM TIC 3X (Leica, Germany) over 6–8 h with an acceleration voltage of 5/4/5 kV. Ion milling was used as it produces a smoother surface than cryotoming ($R_a = 0.23$ nm on the SAN matrix) aiding fast scanning over large areas and also appears to induce surface cross-linking of the butadiene particles [26]. The induced cross-linking reduces the adhesion of the butadiene particles and increases their stiffness, improving scan stability [27].

2.2. Atomic force microscopy

Nanoscale images of surface mechanical properties were acquired in amplitude modulated-frequency modulated (AM-FM) mode [28] using a Cypher ES (Asylum Research, USA) atomic force microscope (AFM) across the weld region of the thin-walled cylindrical samples to observe changes in properties and distribution of the butadiene particles, if any, at the weld interface. Measurements were acquired at room temperature with a silicon cantilever (AC240, Olympus) with a nominal tip radius, R of 7 nm that was driven using photothermal excitation (BlueDriveTM, Asylum Research, USA) to excite the 1st and 2nd eigenmodes of the cantilever simultaneously. AM-FM is used for its capability to obtain highly sensitive property measurements and resolution while maintaining low forces. The reduced elastic punch modulus, E_R (Eq. (1)) and loss tangent, E_R (Eq. (2)) were calculated according to Labuda et al. [29]. and Proksch et al. [30] respectively.

$$E_R = \frac{\pi}{\sqrt{6a}} \left(2k_2 \frac{\Delta f_2}{f_2} \right)^{1.5} \left(\frac{k_1}{Q_1} \frac{A_{0,1}}{A_1} \cos \phi_1 \right)^{-0.5} \tag{1}$$

$$\tan \varphi = \frac{A_1 / A_{0,1} - \sin \phi_1}{\cos \phi_1}$$
 (2)

where a is the punch contact radius, A_1 is the amplitude of the first eigenmode, k_2 is the effective stiffness of the 2nd eigenmode, Δf_2 and f_2 are the frequency shift and resonant frequency respectively of the 2nd eigenmode, k_1 is the stiffness of the 1st eigenmode, Q_1 is the quality factor of the 1st eigenmode, $A_{0,1}$ and A_1 is the free-air amplitude and amplitude setpoint of the 1st eigenmode respectively and ϕ_1 is the phase shift of the first eigenmode. As imaging of the butadiene domains only requires E_R to be qualitative in nature, a is adjusted such that the E_R measurements meets the expected ≈ 3.5 GPa for the SAN matrix.

For the large-scale imaging, a Dimension Icon AFM (Bruker, USA) was used in conjunction with a sub-resonant tapping mode (PeakForce QNM TM , Bruker, USA) to image the bulk samples. A Bruker TESPA-V2 cantilever was used which has a nominal cantilever stiffness, resonant frequency and tip radius of 40 N/m, 300 kHz and \sim 10 nm respectively. Before scans were taken, the deflection sensitivity was calibrated using a hard contact calibration, the spring constant was calibrated using the Sader method [31,32] and the tip radius was calibrated using a Titanium roughness sample (Bruker AFM Probes, USA). For PeakForce QNM, the size of the indentation is typically controlled by setting a maximum

applied load, or peak force. Here, a peak force of 40 nN was used with an oscillation amplitude of 75 nm.

From the indentation, contact mechanics can be used to fit acquired force curves and obtain a map of elastic modulus. Due to ion milling significantly reducing the adhesion of the butadiene particles and the glassy SAN matrix, the DMT (Derjaguin-Muller-Toporov) contact mode [33] is used here to measure the elastic modulus of the indented material as shown

$$F = \frac{4}{3} E_R \sqrt{R} \delta^{1.5} + F_{adh} \tag{3}$$

where F is the applied load, R is the tip radius, δ is the indentation depth, $F_{\rm adh}$ is the adhesive pull-off force and E_R is the reduced modulus. The modulus of the indented material can then be calculated

$$E_R = \frac{1 - \nu_s^2}{E_r} + \frac{1 - \nu_l^2}{E_r} \tag{4}$$

where ν_s , E_s , ν_i and E_i , are the Poisson's ratio and elastic modulus for sample and the indenter tip respectively. While the DMT contact model does not consider viscoelastic effects and assumes a Hertzian relationship between contact radius and indentation depth, it should be sufficient for a qualitative mapping of ABS microstructure since the differences in moduli between the SAN matrix and polybutadiene particles is sufficiently wide at room temperature.

2.3. Tear testing

Tear testing of the weld strength in the cylindrical sample was conducted following the protocol outlined in [9]. For tear testing, 5 samples were cut from the printed cylinder to be 5 mm wide and 60 mm long with the fiber direction aligned with the long axis of the sample. A pre-crack was initiated along a weld in the center of the sample using a sharp razor.

Tear testing was conducted using an RSA G2 DMA (TA Instruments, USA). Samples were pulled at a constant rate of 50 mm/min to induce Mode III crack growth along the weld until the weld had completely torn. Tear resistance was calculated according to

$$T = \frac{2F}{w} \tag{5}$$

where F is the average force during stable tearing and w is the width of the weld. The nominal tearing energy and true tearing energy were calculated using the overall wall thickness ($w_0 = 713 \pm 5 \, \mu \text{m}$) and the actual weld thickness ($w_t = 551 \pm 11 \, \mu \text{m}$) respectively. Optical microscopy was used to quantify the cylinder wall cross-section as shown in Fig. 2 for a tearing specimen. The total weld thickness, w_t is calculated via $w_t = w_t^1 + w_t^2$. The measurements of weld thickness and nominal thickness are conducted across 10 consecutive layers.

3. Results and discussion

Using nanomechanical AFM modes, changes in the microstructure of ABS within the weld zone between two printed fibers are examined with the goal of providing better understanding of the impact of microstructure on fracture toughness of printed ABS parts. AFM property maps are presented first in Section 3.1 followed by the quantification of the butadiene particle distribution. Tearing energy measurements on the same cylindrical samples investigated with AFM will be presented in Section 3.2 with a discussion of their correspondence to AFM data discussed in Section 3.1. In Section 3.3, the internal particle structure is investigated with high resolution nanomechanical property maps. Section 3.4 will discuss how the data from thin walled cylindrical specimens developed specifically for tear testing compare to AFM measurements on bulk ABS samples that better represent typical printing conditions.

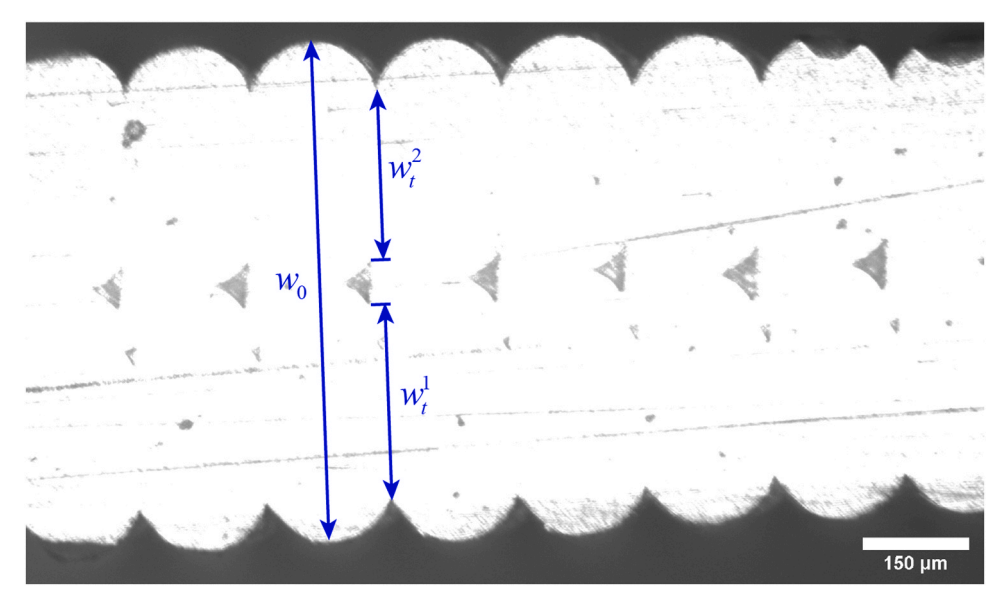


Fig. 2. Cross-section of wall in cylindrical specimen. The nominal width is defined by w_0 which is the maximum distance from edge-to-edge across a single layer. The weld thickness is measured by measuring along the weld line between filaments as indicated by w_t^1 and w_t^2 .

3.1. Weld structure and quantification of butadiene distribution

The regions of a thin walled cylindrical specimen that were imaged using AFM are indicated in the optical image of the sectioned fibers in Fig. 3(a). Maps are acquired at three consecutive weld interfaces, labeled welds 1–3, with the scan areas located at the outer wall of the cylindrical sample. Maps of the measured modulus and loss tangent are provided for each weld in the Fig. 3(b-g). Part of the air gap between fibers is included in the captured image to help locate the weld line between the two layers. The AFM data in each column, Fig. 3(b, e), (c, f) and (d, g) correspond to welds 1, 2 and 3 respectively.

The rubbery butadiene particles are immediately apparent in both the modulus, Fig. 2(b-d), and loss tangent property maps, Fig. 2(e-g), with domain sizes ranging from 40 nm to 1.5 μm. In the modulus maps, the rubbery butadiene particles are significantly softer than the glassy SAN matrix as expected. In the loss tangent maps, the butadiene particles have a significantly higher loss tangent than the glassy SAN matrix and a clear distribution in loss tangent between rubber particles as the domain size decreases is observed. The reduction in the measured loss tangent as the domain size decreases could possibly be due to increased nanoconfinement by the SAN matrix [14], changes in the internal particle morphology [15], or increased substrate effects from the SAN [34]. In both the modulus and loss tangent maps a change in microstructure along the weld line can be observed with the average particle size appearing to decrease near the interface between two subsequent layers. A decrease in particle size across the weld is most clearly observed in the loss tangent channel due to the concomitant color change. Near the air gap (indicated in gray in Fig. 3(b-g)), a decrease in the loss tangent and increase in modulus is observed in the rubber particles possibly due to the diffusion of cyanoacrylate into the ABS during sample preparation.

For quantitative analysis of the domain distribution, the raw modulus maps (Fig. 4(a)) are binarized using Otsu's method [35], followed by a watershed operation [36] to split multiple particles identified as a single region during the binarization process. To convert the binarized property maps into maps of butadiene particle size and distribution a sliding neighborhood filter is used in MATLAB with a predetermined unit square size set to ensure that butadiene particles are always observed within the sliding window. For the example case in Fig. 4(b), the window size, b was set to be 128×128 pixels for a 1024×1024 pixel image. The polybutadiene particles can then be analyzed within the window according to a chosen set of metrics.

Two metrics termed 'area fraction', A and 'domain frequency', c are used to quantify the density of the particles within the sliding window. The area fraction, A is the fraction of pixels within the sliding window that are occupied by a particle, with A=1 indicating that the sliding window is completely occupied by particles and A=0 indicating that no particles are within the sliding window (Fig. 4(c)). The domain frequency, c is the number density of the particle centroids within the sliding window (Fig. 4(d)). A dimensionless measure of the normalized domain size, D_n within the window is calculated using Eq. (6) using the measured A and c within the sliding window.

$$D_c = \frac{A}{c} \tag{6}$$

The results of using the sliding window operations on the modulus maps for each of the welds imaged in Fig. 3 are shown in Fig. 5. In the welds examined, Welds 1 and 3 (Fig. 5(a, d) and (c, f) respectively) show a clear band approximately 5 μ m wide with a lower volume fraction and normalized particle size extending from the air gap and going across the image along the weld line between the two filaments. For Weld 2 some particles near the tip of the air gap (Fig. 5(d, e)) result in high local A and D_c but further along the weld line a decrease in A and D_c is still observed in a region approximately 10 μ m wide. It is noted by the authors that the weld line between the filaments is not necessarily represented by a perfectly straight, vertical line and deviations may occur due to the distribution in contact pressure during printing deforming the already printed filament [10]. Therefore, the path of the butadiene deficient zone can be expected to diverge from the line describing the shortest distance across the interface between two fibers.

A decrease in both A and D_c along the weld lines suggests that during printing under these conditions the weld zone is predominantly comprised of smaller butadiene particles, reducing both the concentration and average size across the weld between the two filaments. The optimal toughness of SAN occurs when there is a bimodal distribution of rubber particles [19,20], and that the average particle diameter is above 300 nm according to some estimates [37,38]. Therefore, a local decrease in the average particle size from the intended distribution would likely decrease the toughness of SAN within the weld zone as there are less sufficiently large particles to induce crazing within the weld zone [37]. To test whether the weld zones imaged have a reduced number of particles with a diameter, D larger than 300 nm the binarized images of each weld were modified to remove particles with D < 300 nm before

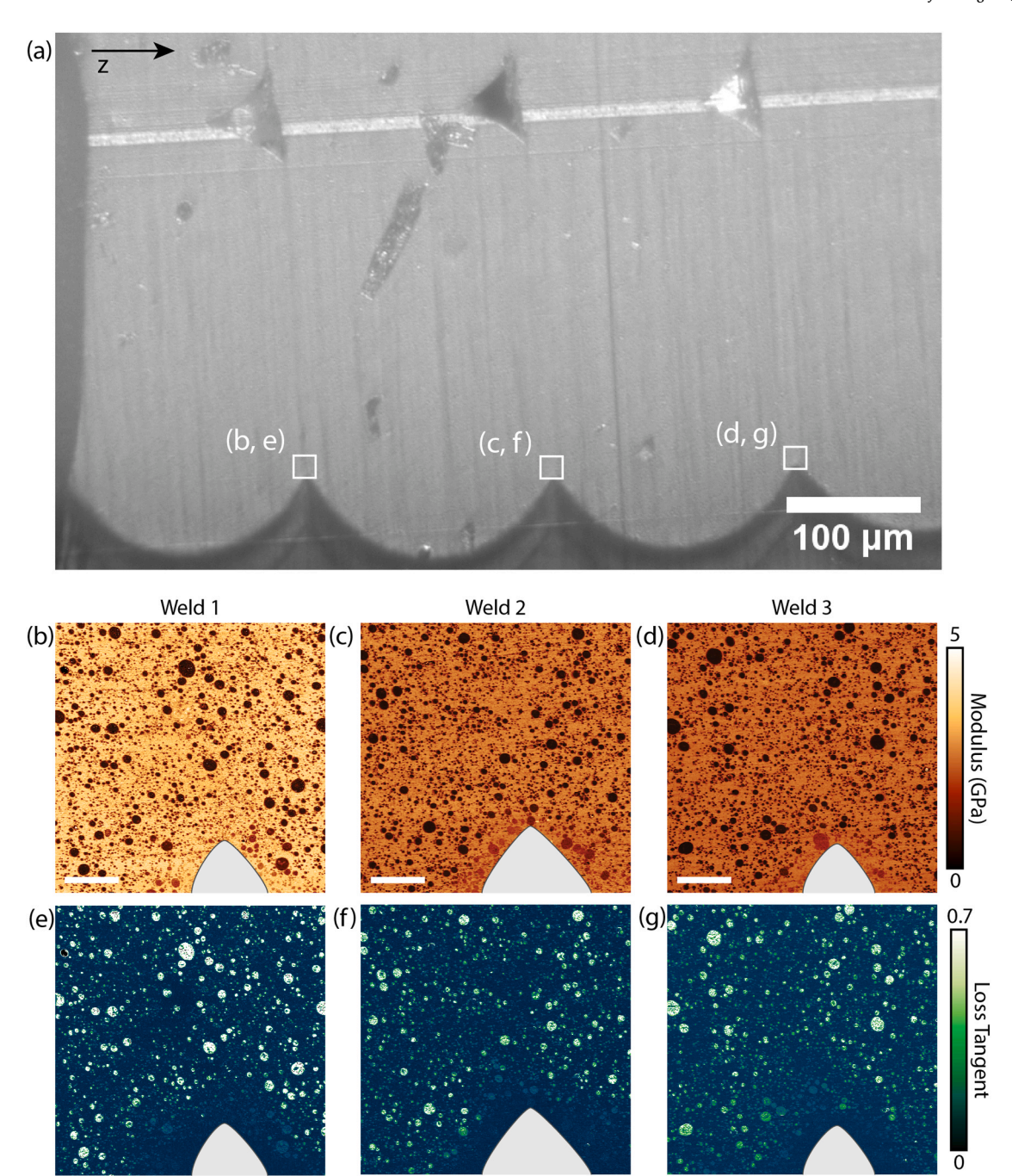


Fig. 3. (a) Optical image of the FFF-ABS cross-section prepared for imaging with AFM. The locations used for AFM imaging are indicated with white squares. The vertical print orientation (*z*-axis) is indicated with a black arrow. (b–d) Punch moduli and (e–g) loss tangent of welds 1–3. Scale bar indicates 4 μm. The air gap between filaments is indicated in gray and is not included in subsequent analysis. The measurement parameters are $A_{0,1} = 283.5$ nm, $A_1 = 204.8$ nm, $f_{0,1} = 66.016$ kHz, $k_1 = 2.72$ N/m $Q_1 = 156.03$, $A_2 = 0.9$ nm, $f_{0,2} = 406.644$ kHz, $k_2 = 62.03$ N/m, $a_1 = 2$ nm.

the domain frequency, c is quantified. The resulting map for each weld is shown in Fig. 5(g–i). In all cases, a decrease in the number of craze-inducing particles (i.e. D>300 nm) can be observed within the butadiene deficient regions identified in Fig. 5. The reduction of particles capable of inducing stable craze formation at low stress is likely to result in more brittle fracture within the welds as unstable craze growth is allowed to initiate at the inter-fiber porosity and propagate across the weld. While previous work has a identified a butadiene deficiency from Raman spectroscopy [24], the use of AFM and quantitative image analysis allows for reduction in average butadiene particle size (which is not measurable with Raman spectroscopy) and density within the weld region to be identified. To confirm that the observed change in

microstructure is associated with decreased weld strength compared to expectations from bulk ABS, trouser tear tests are conducted in the following Section 3.2.

3.2. Impact of structure on fracture toughness

The tearing energies along welds in the same thin-walled cylindrical sample from which the AFM data was collected is presented in Fig. 6(a representative tearing curve is provided in Fig. S1 of the Supporting Information). Nominal tearing energies of 14.3 ± 0.5 N/mm and true tearing energy of 18.5 ± 0.6 N/mm were measured across 5 tearing samples, which are substantially lower than the tearing energy for a bulk

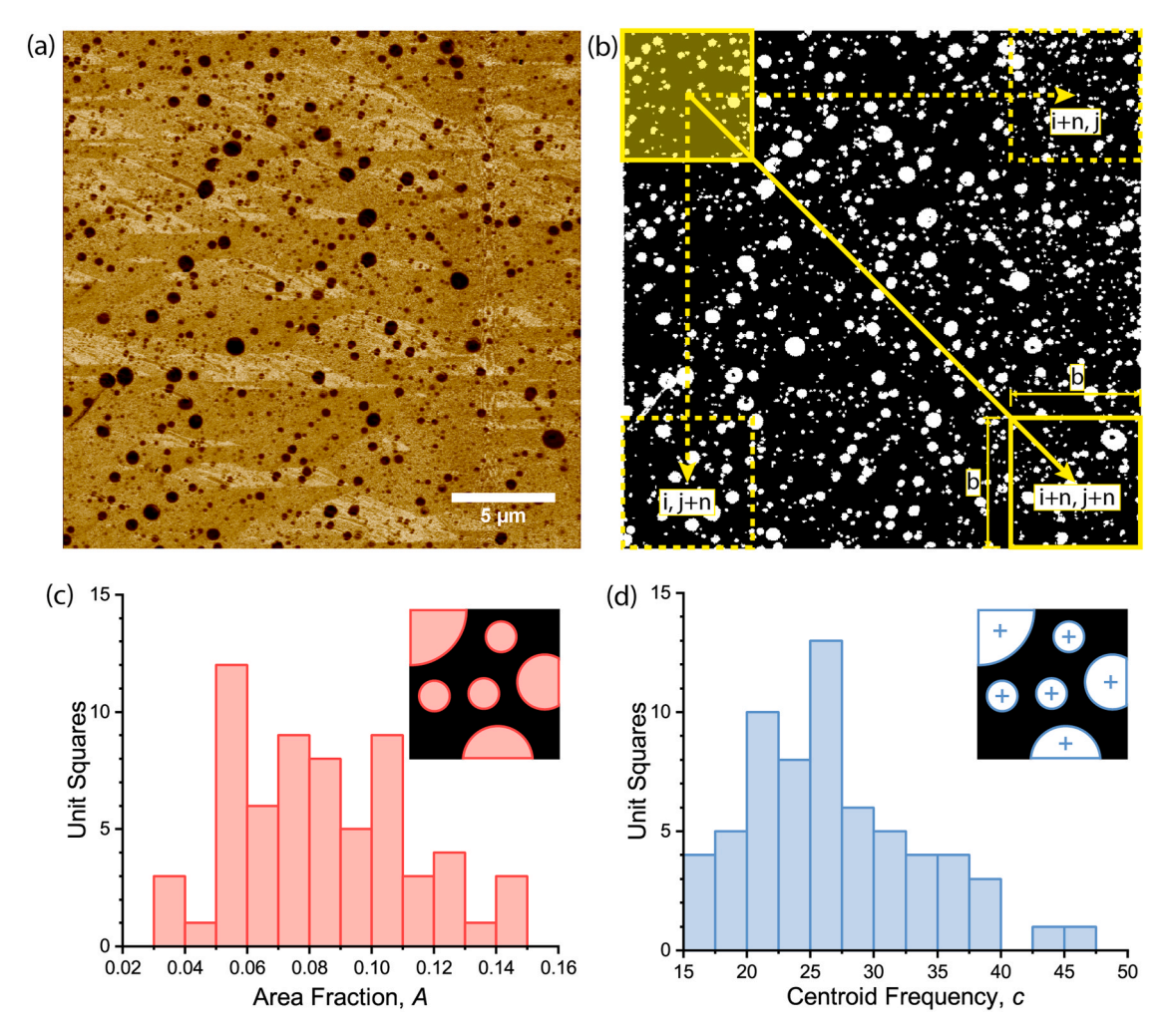


Fig. 4. AFM DMT modulus map in the bulk region of an FFF printed, ABS filament with nominal distribution of polybutadiene particles collected with PeakForce QNM. (b) Binarized version of (a) with a schematized representation of the sliding window used for quantification of the butadiene domain structure included. The sliding window advances 1 pixel at a time and calculates properties within the window. (c) Histogram of the area fraction in each segmented region within (b) occupied by polybutadiene particles. (d) Histogram of particle centroid frequency in (b) by counting the number of centroids in each segmented region.

sample of ABS ($T_0=35.9\pm2.1$ N/mm) [5]. Accounting for the smaller weld width (see Section 2.3) and calculating the true tearing energy improved the estimated weld strength but does not fully account for the loss of mechanical strength compared to the bulk tearing strength of ABS.

The measurement of tearing energy on the thin walled cylindrical sample is in reasonable agreement with the tearing energy measurements by Davis et al. [5] on similarly thin walled FFF-ABS samples (Fig. 6). Differences in the weld strength and spread of measured tearing energy values in this study compared to Davis et. al. can be expected due to differences in the exact printing conditions and subsequent changes in thermal history between the layers. The measured true tearing energy at all printing temperatures is lower than bulk ABS, suggesting that the observed microstructural changes in our sample may also explain the reduction in tearing energy in Davis et al. samples. The reduction in tearing strength with decreasing nozzle temperature could be explained by the faster cooling preventing migration of large butadiene particles into the weld zone but further work is needed to uncover the exact physical mechanism causing the deficiency in butadiene within the weld. One possible explanation is that a SAN-rich shell forms during extrusion of the filament and during weld formation the cross-linked particles have insufficient mobility to migrate through the SAN-rich shell into the weld formed between filaments in the time that the SAN remains mobile.

Other measurements of the strength of FFF-ABS specimens have also shown a decrease in fracture toughness [22,23,39] and ultimate tensile strength [21] for FFF-ABS compared to injection molded specimens as previously discussed. Compared to the tearing measurements, bulk measurements are indirect measurements of weld strength and incorporate the mesostructure of the printed component in the mechanical response. The role of the mesostructure in fracture behavior of bulk FFF specimens convolutes the relationship between processing, microstructure and fracture properties which will require additional analysis methods before direct comparisons can be made to weld tearing measurements.

Compounding the effect of the altered microstructure within the weld on the fracture toughness is the presence of the notch between the filaments. The notch that is present here (and in bulk samples as interlayer porosity) in FFF structures (Fig. 1) can act as a stress concentration and crack initiation site, allowing preferential crack formation within the weld zone (Fig. 7(a)) at lower stress that what is expected from traditionally manufactured ABS [40]. Further, observation of a fracture near the notch (Fig. 7(b and c)) between the two printed fibers indicates that the crack growth does not necessarily occur along a straight path. A clear deviation can be observed in Fig. 7(b), suggesting that crack growth may in fact occur through the path of least resistance (possibly defined by the local butadiene microstructure) after being initiated at a notch or porosity in bulk samples. Understanding the relative

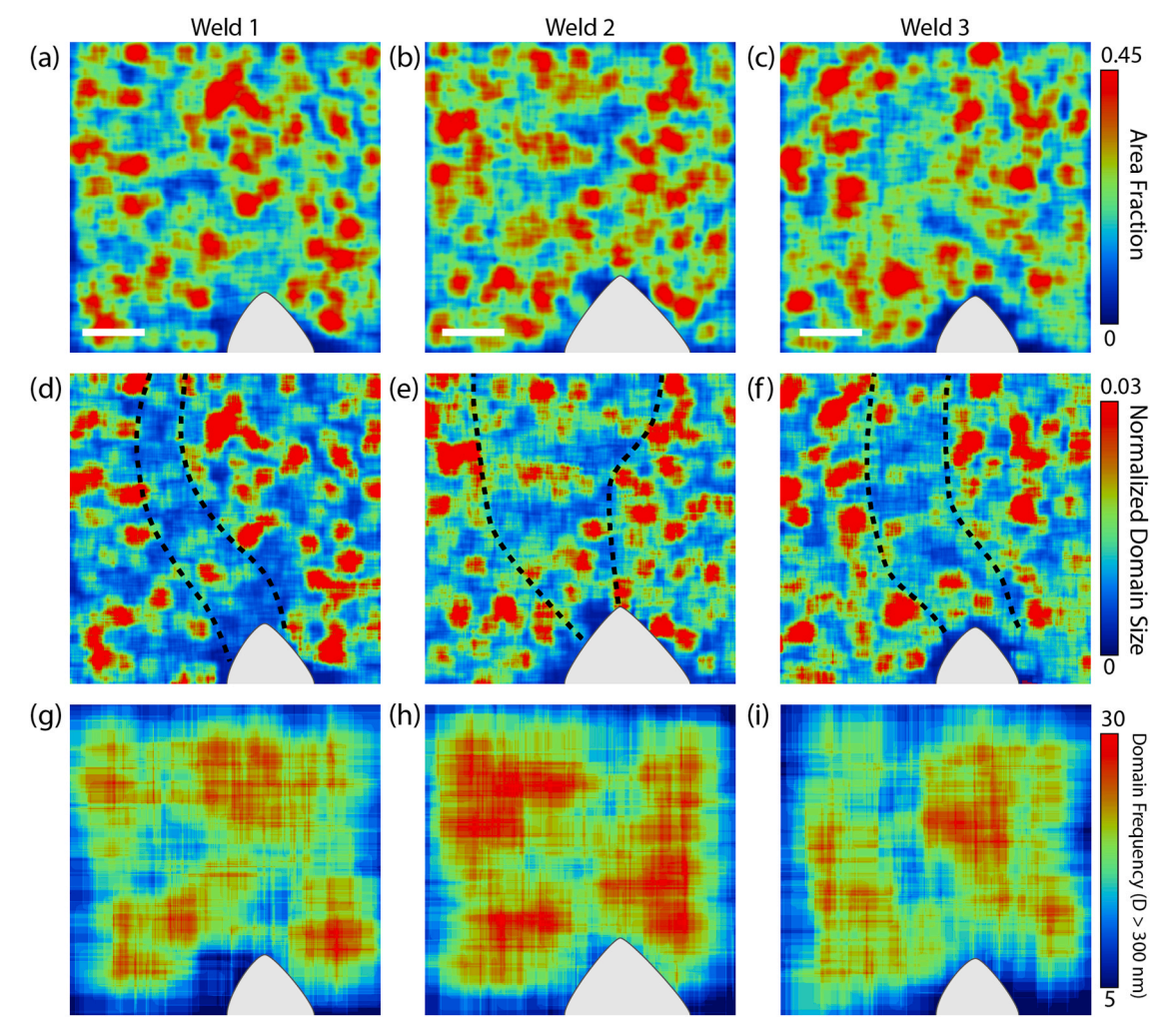


Fig. 5. Quantification of butadiene distribution and domain size in the property maps from Fig. 3. (a–c) Maps of the local area fraction (A), (d–f) normalized domain size (D_c), and (g–i) number density of particles (c) with D > 300 nm for Welds 1–3 as labeled. Scale bar indicates 4 μ m. The acquired scan was 512 \times 512 pixels. A 32 \times 32 pixel window is used for the neighborhood operation to calculate A and D_c . A 128 \times 128 pixel window is used for the neighborhood operation to calculate the number density of particles with D > 300 nm. The dashed lines are a guide to the eye for indicating the deficient region.

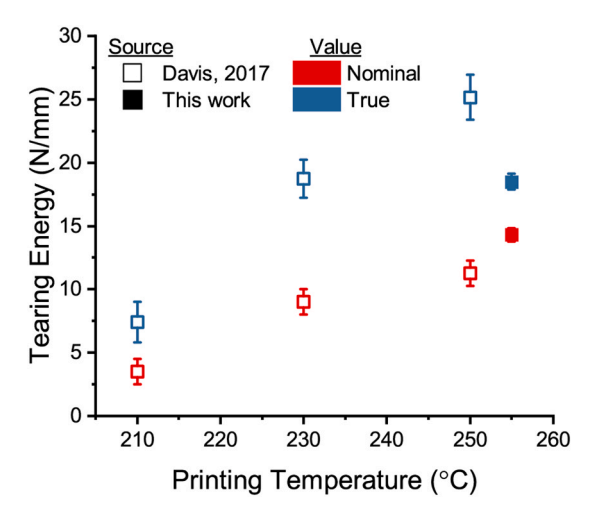


Fig. 6. Comparison of the measured tearing energy of the cylindrical samples used in this study compared to the measurements made by Davis et al. The error is the standard distribution of tearing energy across 5 samples and includes the standard deviation of the variance during the steady state tearing of a single test.

contributions of the notch and the weld microstructure on the overall strength will require further investigation with simulation and carefully controlled experiments. The difference for injection molded ABS components or other conventional manufacturing techniques compared to FFF is that while there may be changes in the butadiene distribution near the surface of conventionally manufactured ABS parts, they are not filled with internal porosity and butadiene deficient zones that are detrimental to the fracture toughness and instead have a relatively homogenous dispersion of butadiene throughout.

3.3. Internal butadiene particle structure

High resolution mapping of individual particle structure indicates dual particle morphologies within the ABS studied here. Larger 'salami' particles with SAN inclusions can be observed in Fig. 8(a–c) as well as smaller, more homogenous particles that dispersed throughout the matrix. In addition, some small angular particles that exhibit high modulus can be observed, which is likely the Titanium Oxide used as a white pigment for the filament. Examination of the 1st eigenmode amplitude map in Fig. 8(a) provides the best visualization of the internal particle structure. The reduced modulus map (Fig. 8(b)) shows much lower modulus on the rubber particles compared to the matrix as expected, but is still several orders of magnitude larger relative to expectations for typical nitrile butadiene rubber properties (E=1–10 MPa)

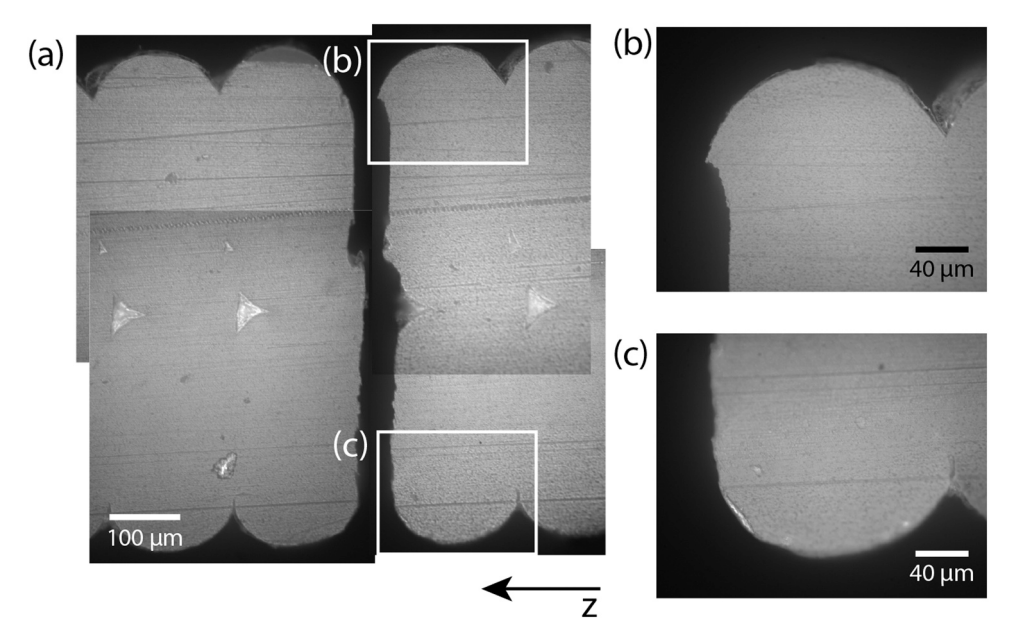


Fig. 7. (a) Optical image of a fracture induced by Mode I loading (tension) in the thin walled cylindrical sample. The vertical (*z*) print direction is indicated. (b and c) Detail image of the crack at the notch between the two filaments on the (b) outside wall and (c) inside wall.

due to limitations of Hertzian contact mechanics in the analysis of soft, adhesive polymers [41,42]. For the purposes of this study, an accurate, quantitative measurement of the butadiene particle moduli is not necessary as we are only interested in the distribution of the particles themselves and their impact on bulk fracture properties. Measurement of the loss tangent (Fig. 8(c)) shows significantly higher damping on the rubber particles than the glassy SAN matrix as expected, with the SAN inclusions within the 'salami' rubber particles also showing a smaller loss tangent. As is observed in Fig. 3, the smaller rubber particles show a much lower loss tangent than the salami particles. Some variation in loss tangent is also observed within the smaller particle set, possibly due to the greater confinement by the stiff SAN matrix as suggested previously in Section 3.1.

Imaging an isolated large particle allows for detailed characterization of the internal particle microstructure (Fig. 8(d and e)). Only minor variation in modulus is observed despite the SAN inclusions, likely due to the elastic foundation [43] provided by the soft rubber causing the inclusions to easily deflect under load reducing modulus contrast. At certain points, the complicated contact conditions cause non-physical data to be collected, observable as black regions in Fig. 8(d). In comparison, calculation of the dissipated energy from the 1st eigenmode yields excellent internal contrast, likely due to the differences in adhesion between the inclusions and the surrounding rubber. The adhesive, viscoelastic rubber shows high dissipation, with much lower dissipated energy measurements made on the inclusions and the surrounding matrix. Here it is demonstrated that AM-FM AFM is highly capable of characterizing rubber particle structure in-situ and will be beneficial for studying rubber phase morphology and properties. Future work that focuses on accurately quantifying the butadiene mechanical properties would require quasi-static AFM techniques that can incorporate adhesive contact mechanics. In addition, a means to account for the finite size of the butadiene particles and the substrate effect from the surrounding SAN through analytical corrections or finite element analysis would be needed to account for the changing particle sizes.

The change in morphology between the large and small particles observed in the high-resolution analysis supports the suggestion made in Section 3.1 that both large and small particles are required for optimal weld fracture toughness with the 'salami' nature of the large particles known to be beneficial for the toughening properties of large particles [15]. Development of an ABS that can exhibit improved weld strength

with FFF may require particles that can toughen a SAN matrix under a wider range of size distributions and concentrations which may involve modifying internal particle morphology.

3.4. Weld microstructure in a bulk sample

The data thus far has examined thin-walled samples in order to isolate the welds for tear testing and simplify the thermal history. Yet, most parts are constructed from FFF as bulk parts, and therefore a comparison of the weld zone in a bulk sample (Fig. 9) to the earlier thinwalled sample is performed. The bulk weld zone shows a thinner region approximately 3 µm wide (compared to approximately 4-10 µm in the thin-walled sample welds) where the local A and D_c is smaller than the bulk of the printed fibers. The use of PeakForce QNM allows for a larger $50 \times 50 \ \mu m$ scan of the weld and surrounding area as shown in raw DMT modulus channel in Fig. 9(a), which shows a similar microstructure as the AM-FM property maps in Fig. 8. Quantification of the area fraction (Fig. 9(b)) and the normalized domain size (Fig. 9(c)) of a weld zone (complete maps of the area shown in Fig. 9(a) are provided in Fig. S2 in the Supplementary Information) in the bulk sample indicates that the butadiene distribution remains biased towards smaller values of A and D_c across the weld, but the change is not as dramatic as for the thin walled sample in Fig. 3.

Imaging additional welds within the bulk specimen continues to show a reduced butadiene deficient region within the weld zone compared to the thin-walled cylindrical sample (see Fig. S3 in the Supporting Information for another example of a weld in the bulk sample). However, as the ultimate tensile strength of a FFF part is defined by its weakest load bearing interfaces, the existence of any welds in a bulk sample with polybutadiene deficient zones provides a microstructural cause for the brittle fracture behavior when loaded across the welds [22]. Further, the bulk sample tested here only represents one printing configuration and Raman spectroscopy data [24] has suggested that the extent of the butadiene deficient region is dependent on print configuration. Future work on bulk specimens will aim to extend testing of weld microstructure for different print configurations to understand the role of print geometry and thermal history.

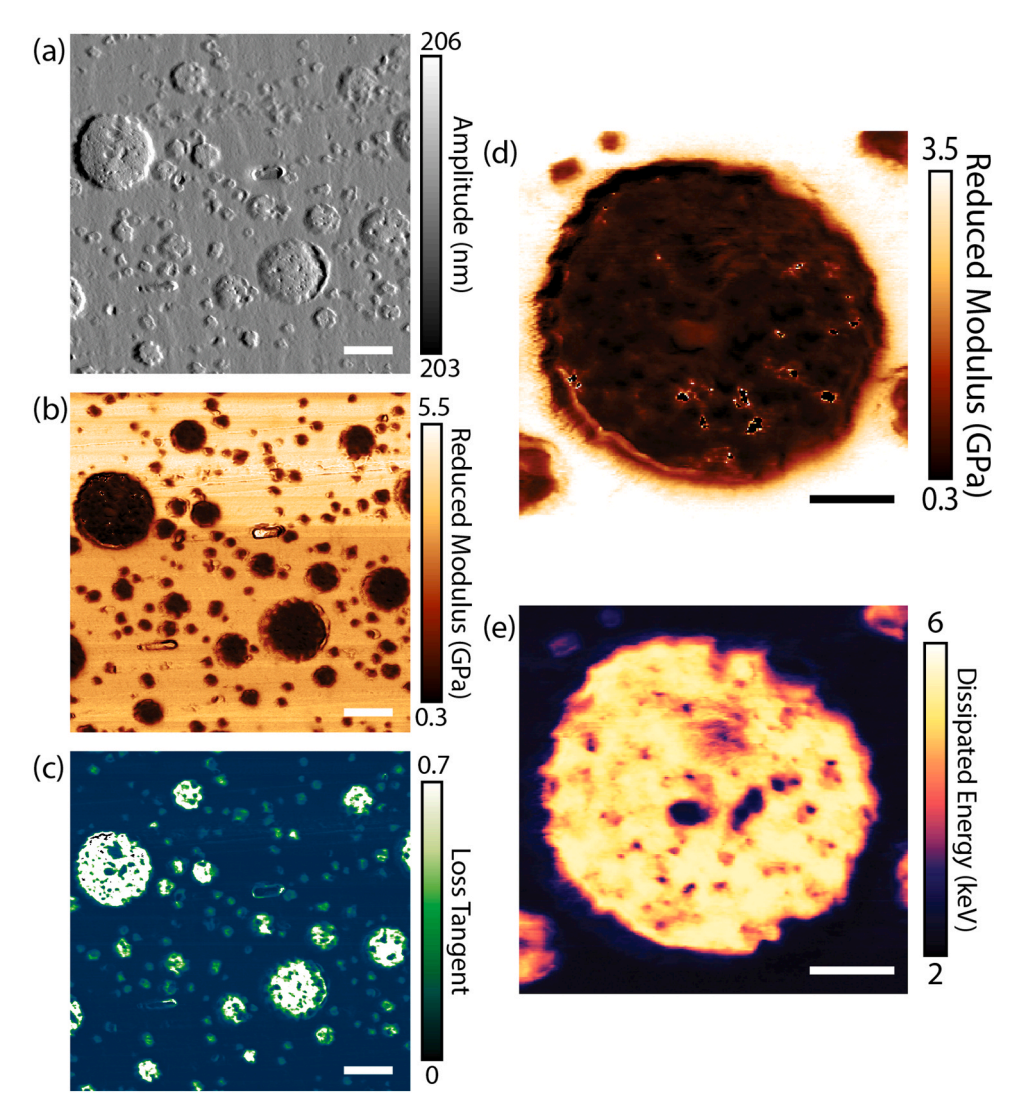


Fig. 8. (a–c) AM-FM property maps of polybutadiene particles in ABS: (a) Amplitude of the first eigenmode, (b) Punch Modulus, and (c) Loss Tangent. (d–e) Internal structure and stiffness of a single latex polybutadiene particle: (d) Punch modulus and (e) dissipated energy from the first eigenmode. The scale bar in (a–c) indicates 500 nm. The scale bar in (d–e) indicates 200 nm. The measurement parameters are the same as for Fig. 3.

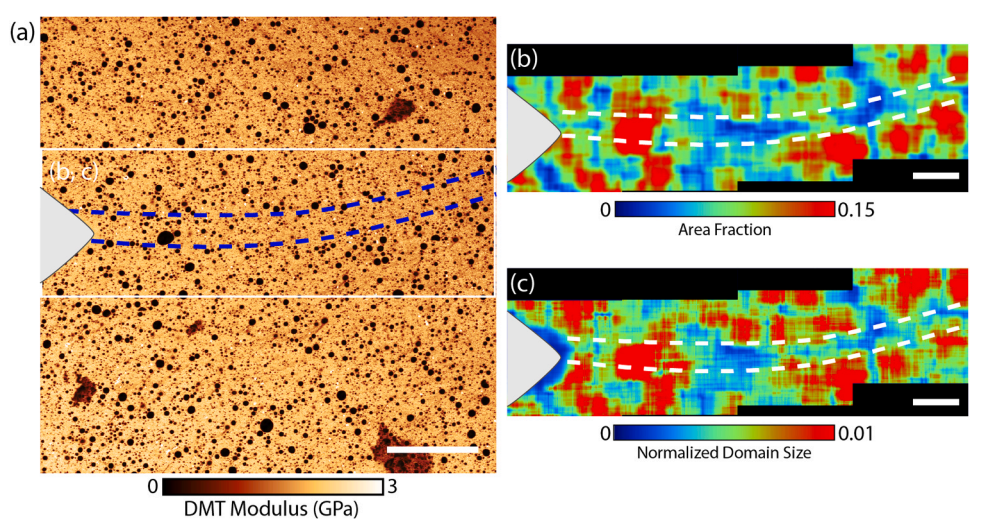


Fig. 9. DMT modulus map across the weld region in a bulk sample. (a) DMT modulus map across a single weld region. The air gap between filaments, which is excluded in the analysis, is indicated in gray. The blue dashed lines are a guide to the eye for indicating the deficient region. The white scale bar indicates $10~\mu m$. Detailed quantitative maps of (b) local area fraction (c) normalized domain size across the weld region indicated in (a). The scale bar indicates $5~\mu m$. (For interpretation of the references to color in this figure legend, the reader is referred to the web version of this article.)

4. Conclusions

Nanomechanical AFM analysis of fused filament fabricated (FFF) ABS samples was conducted to map the distribution of the nitrilebutadiene particles within the weld zone between printed fibers. High resolution nanomechanical mapping successfully identified the rubber particles within the weld region for a thin-walled cylindrical sample. From collected AFM data, the local distribution of the rubber particles within the weld region was assessed by quantifying the particle density and average size within a sliding window. In all welds imaged, a decrease in the density and average size of the rubber particles within the neck region was directly observed. These findings suggest that the decrease in the average size and density of nitrile-butadiene particles is one factor that can reduce fracture toughness of FFF-ABS by limiting the particle induced crazing that is responsible for the toughness of traditional ABS parts. The changes in microstructure observed in this study are consistent with the brittle fracture behavior observed in FFF specimens here and throughout literature that has not previously been connected to a microstructural origin. The role of porosity in fracture initiation and growth has also been recently investigated in FFF parts and shown to be significant. The interaction between the distribution of butadiene particles, part mesostructure and resulting fracture toughness needs further investigation before a direct relationship between weld microstructure and the bulk fracture toughness of FFF-ABS can be

To improve the structural integrity of the weld region in FFF-ABS parts, further work is needed to understand the migration of the polybutadiene particles through the SAN matrix during printing and to ensure that the polybutadiene particles can distribute uniformly throughout the neck region in FFF. Annealing has already been demonstrated as a means to improve the fracture toughness of FFF-ABS parts, possibly due to allowing the larger butadiene particles to migrate into the weld zone. Principles from the significant work conducted on the migration of particles in viscoelastic fluids [44] may provide a means to predict the migration of the butadiene particles during weld formation and the required effective weld time [9] for tough welds to form during printing.

CRediT authorship contribution statement

David W. Collinson: Conceptualization, Methodology, Software, Validation, Formal analysis, Investigation, Writing - original draft, Visualization. Pavan V. Kolluru: Methodology, Investigation, Writing - review & editing. Natalia Von Windheim: Methodology, Investigation, Visualization, Writing - review & editing. L. Catherine Brinson: Conceptualization, Resources, Supervision, Project administration, Funding acquisition, Writing - review & editing.

Declaration of Competing Interest

The authors declare that they have no known competing financial interests or personal relationships that could have appeared to influence the work reported in this paper.

Acknowledgements

This multi-year research effort was sequentially supported by grants from the National Science Foundation (NSF): CMMI-1818574, BCS-1734981 and by The Goodyear Tire & Rubber Company. DWC was partially supported by Fulbright Science and Innovation Fellowship, the John R Templin Fellowship and the Ryan Fellowship from the International Institute for Nanotechnology (IIN). NV was supported by Duke University, Award Number: 291-0067. This work made use of the EPIC facility of Northwestern University's NUANCE Center, which has received support from the SHyNE Resource (NSF ECCS-2025633), the IIN, and Northwestern's Materials Research Science and Engineering

Center (MRSEC) program (NSF DMR-1720139). This work was also performed in part at the Duke University Shared Materials Instrumentation Facility (SMIF), a member of the North Carolina Research Triangle Nanotechnology Network (RTNN), which is supported by the National Science Foundation (award number ECCS-2025064) as part of the National Nanotechnology Coordinated Infrastructure (NNCI). The funding sources were not involved in any aspect of this study.

Appendix A. Supporting information

Supplementary data associated with this article can be found in the online version at doi:10.1016/j.addma.2021.101964.

References

- [1] T.D. Ngo, A. Kashani, G. Imbalzano, K.T.Q. Nguyen, D. Hui, Additive manufacturing (3D printing): a review of materials, methods, applications and challenges, Compos. Part B Eng. 143 (2018) 172–196.
- [2] M. Vaezi, H. Seitz, S. Yang, A review on 3D micro-additive manufacturing technologies, Int. J. Adv. Manuf. Technol. 67 (5) (2013) 1721–1754.
- [3] M.S. Uddin, M.F.R. Sidek, M.A. Faizal, R. Ghomashchi, A. Pramanik, Evaluating mechanical properties and failure mechanisms of fused deposition modeling acrylonitrile butadiene styrene parts, J. Manuf. Sci. Eng. 139 (8) (2017).
- [4] Q. Sun, G.M. Rizvi, C.T. Bellehumeur, P. Gu, Effect of processing conditions on the bonding quality of FDM polymer filaments, Rapid Prototyp. J. 14 (2) (2008) 72–80.
- [5] C.S. Davis, K.E. Hillgartner, S.H. Han, J.E. Seppala, Mechanical strength of welding zones produced by polymer extrusion additive manufacturing, Addit. Manuf. 16 (2017) 162–166.
- [6] M. Kaveh, M. Badrossamay, E. Foroozmehr, A. Hemasian Etefagh, Optimization of the printing parameters affecting dimensional accuracy and internal cavity for HIPS material used in fused deposition modeling processes, J. Mater. Process. Technol. 226 (2015) 280–286.
- [7] S. Ziemian, M. Okwara, W. Ziemian Constance, Tensile and fatigue behavior of layered acrylonitrile butadiene styrene, Rapid Prototyp. J. 21 (3) (2015) 270–278.
- [8] A.K. Sood, R.K. Ohdar, S.S. Mahapatra, Parametric appraisal of mechanical property of fused deposition modelling processed parts, Mater. Des. 31 (1) (2010) 287-295
- [9] J.E. Seppala, S. Hoon Han, K.E. Hillgartner, C.S. Davis, K.B. Migler, Weld formation during material extrusion additive manufacturing, Soft Matter 13 (38) (2017) 6761–6769
- [10] T.J. Coogan, D.O. Kazmer, Prediction of interlayer strength in material extrusion additive manufacturing, Addit. Manuf. 35 (2020), 101368.
- [11] M.A.G. Cunha, M.O. Robbins, Effect of flow-induced molecular alignment on welding and strength of polymer interfaces, Macromolecules 53 (19) (2020) 8417–8427.
- [12] J. Yin, C. Lu, J. Fu, Y. Huang, Y. Zheng, Interfacial bonding during multi-material fused deposition modeling (FDM) process due to inter-molecular diffusion, Mater. Des. 150 (2018) 104–112.
- [13] C.B. Bucknall, I.K. Partridge, M.V. Ward, Rubber toughening of plastics, JMatS 19 (6) (1984) 2064–2072.
- [14] J. Wang, X. Zhang, L. Jiang, J. Qiao, Advances in toughened polymer materials by structured rubber particles, Prog. Polym. Sci. 98 (2019), 101160.
- [15] C.B. Bucknall, Rubber toughening, in: R.N. Haward, R.J. Young (Eds.), The Physics of Glassy Polymers, Springer Netherlands, Dordrecht, 1997, pp. 363–412.
- [16] A.S. Argon, The Physics of Deformation and Fracture of Polymers, Cambridge University Press, Cambridge, 2013.
- [17] A. Pfau, A. Janke, W. Heckmann, Determination of the bulk structure of technical multiphase polymer systems with AFM: comparative AFM and TEM investigation, Surf. Interface Anal. 27 (5–6) (1999) 410–417.
- [18] C. Bucknall, Toughened Plastics, Springer Netherlands, Dordrecht, 1977.
- [19] M.E. Fowler, H. Keskkula, D.R. Paul, Synergistic toughening in rubber modified blends, Poly 28 (10) (1987) 1703–1711.
- [20] M.E. Fowler, H. Keskkula, D.R. Paul, Mechanical behavior of dual-rubber-modified SAN, J. Appl. Polym. Sci. 35 (6) (1988) 1563–1571.
- [21] A.M. Peterson, Review of acrylonitrile butadiene styrene in fused filament fabrication: a plastics engineering-focused perspective, Addit. Manuf. 27 (2019) 363–371.
- [22] K.R. Hart, E.D. Wetzel, Fracture behavior of additively manufactured acrylonitrile butadiene styrene (ABS) materials, EnFM 177 (2017) 1–13.
- [23] K.R. Hart, R.M. Dunn, J.M. Sietins, C.M. Hofmeister Mock, M.E. Mackay, E. D. Wetzel, Increased fracture toughness of additively manufactured amorphous thermoplastics via thermal annealing, Poly 144 (2018) 192–204.
- [24] D.P. Cole, J.C. Riddick, H.M. Iftekhar Jaim, K.E. Strawhecker, N.E. Zander, Interfacial mechanical behavior of 3D printed ABS, J. Appl. Polym. Sci. 133 (30) (2016).
- [25] A. International, ASTM D638-14, Standard Test Method for Tensile Properties of Plastics, West Conshohocken, PA, 2014.
- [26] R.L. Bruce, S. Engelmann, T. Lin, T. Kwon, R.J. Phaneuf, G.S. Oehrlein, B.K. Long, C.G. Willson, J.J. Végh, D. Nest, D.B. Graves, A. Alizadeh, Study of ion and vacuum ultraviolet-induced effects on styrene- and ester-based polymers exposed to argon plasma, J. Vac. Sci. Technol. B Microelectron. Nanometer Struct. Process. Meas. Phenom. 27 (3) (2009) 1142–1155.

- [27] R. García, Dynamic atomic force microscopy methods, Surf. Sci. Rep. 47 (6–8) (2002) 197–301.
- [28] M. Kocun, A. Labuda, W. Meinhold, I. Revenko, R. Proksch, Fast, high resolution, and wide modulus range nanomechanical mapping with bimodal tapping mode, ACS Nano 11 (10) (2017) 10097–10105.
- [29] A. Labuda, M. Kocun, W. Meinhold, D. Walters, R. Proksch, Generalized Hertz model for bimodal nanomechanical mapping, Beilstein J. Nanotechnol. 7 (2016) 970–982.
- [30] R. Proksch, D.G. Yablon, Loss tangent imaging: theory and simulations of repulsive-mode tapping atomic force microscopy, Appl. Phys. Lett. 100 (7) (2012) 073106/1–3.
- [31] J.E. Sader, J.W.M. Chon, P. Mulvaney, Calibration of rectangular atomic force microscope cantilevers, Rev. Sci. Instrum. 70 (10) (1999) 3967–3969.
- [32] J.E. Sader, J.A. Sanelli, B.D. Adamson, J.P. Monty, X. Wei, S.A. Crawford, J. R. Friend, I. Marusic, P. Mulvaney, E.J. Bieske, Spring constant calibration of atomic force microscope cantilevers of arbitrary shape, Rev. Sci. Instrum. 83 (10) (2012) 103705/1–10370516.
- [33] B.V. Derjaguin, V.M. Muller, Y.P. Toporov, Effect of contact deformations on the adhesion of particles, J. Colloid Interface Sci. 53 (2) (1975) 314–326.
- [34] L. Li, L.M. Encarnacao, K.A. Brown, Polymer nanomechanics: separating the size effect from the substrate effect in nanoindentation, Appl. Phys. Lett. 110 (4) (2017) 043105/1–043105/5.
- [35] N. Otsu, A threshold selection method from gray-level histograms, IEEE Trans. Syst. Man Cybern. 9 (1) (1979) 62–66.

- [36] L. Vincent, P. Soille, Watersheds in digital spaces: an efficient algorithm based on immersion simulations, ITPAM 13 (6) (1991) 583–598.
- [37] Y. Han, R. Lach, W. Grellmann, Effects of rubber content and temperature on unstable fracture behavior in ABS materials with different particle sizes, J. Appl. Polym. Sci. 79 (1) (2001) 9–20.
- [38] Y. Deng, G. Gao, Z. Liu, C. Cao, H. Zhang, Co-toughened polystyrene by submicrometer-sized core-shell rubber particles and micrometer-sized salami rubber particles, Ind. Eng. Chem. Res. 52 (14) (2013) 5079–5084.
- [39] J.C. Riddick, M.A. Haile, R.V. Wahlde, D.P. Cole, O. Bamiduro, T.E. Johnson, Fractographic analysis of tensile failure of acrylonitrile-butadiene-styrene fabricated by fused deposition modeling, Addit. Manuf. 11 (2016) 49–59.
- [40] K.M. Conway, G.J. Pataky, Crazing in additively manufactured acrylonitrile butadiene styrene, EnFM 211 (2019) 114–124.
- [41] D. Maugis, Adhesion of spheres: the JKR-DMT transition using a dugdale model, J. Colloid Interface Sci. 150 (1) (1992) 243–269.
- [42] D.C. Lin, F. Horkay, Nanomechanics of polymer gels and biological tissues: a critical review of analytical approaches in the Hertzian regime and beyond, Soft Matter 4 (4) (2008) 669–682.
- [43] T. Ohashi, T. Sato, T. Nakajima, P. Junkong, Y. Ikeda, Necessity of two-dimensional visualization of validity in the nanomechanical mapping of atomic force microscopy for sulphur cross-linked rubber, RSC Adv. 8 (57) (2018) 32930–32941.
- [44] D. Yuan, Q. Zhao, S. Yan, S.-Y. Tang, G. Alici, J. Zhang, W. Li, Recent progress of particle migration in viscoelastic fluids, LChip 18 (4) (2018) 551–567.